

IMAGES[★] I. Strong evolution of galaxy kinematics since $z = 1$

Y. Yang¹, H. Flores¹, F. Hammer¹, B. Neichel¹, M. Puech², N. Nesvadba¹, A. Rawat^{1,3}, C. Cesarsky², M. Lehnert¹, L. Pozzetti⁴, I. Fuentes-Carrera¹, P. Amram⁵, C. Balkowski¹, H. Dannerbauer⁶, S. di Serego Alighieri⁷, B. Guiderdoni⁸, A. Kembhavi³, Y. C. Liang⁹, G. Östlin¹⁰, C. D. Ravikumar¹¹, D. Vergani¹², J. Vernet², and H. Wozniak⁸

¹ GEPI, Observatoire de Paris, CNRS, University Paris Diderot; 5 Place Jules Janssen, Meudon, France

² ESO, Karl-Schwarzschild-Strasse 2, D-85748 Garching bei München, Germany

³ Inter-University Centre for Astronomy and Astrophysics, Post Bag 4, Ganeshkhind, Pune 411007, India

⁴ INAF - Osservatorio Astronomico di Bologna, via Ranzani 1, 40127 Bologna, Italy

⁵ Laboratoire d'Astrophysique de Marseille, Observatoire Astronomique de Marseille-Provence, 2 Place Le Verrier, 13248 Marseille, France

⁶ MPIA, Königstuhl 17, D-69117 Heidelberg, Germany

⁷ INAF, Osservatorio Astrofisico di Arcetri, Largo Enrico Fermi 5, I-50125, Florence, Italy

⁸ Centre de Recherche Astronomique de Lyon, 9 Avenue Charles Andr, 69561 Saint-Genis-Laval Cedex, France

⁹ National Astronomical Observatories, Chinese Academy of Sciences, 20A Datun Road, Chaoyang District, Beijing 100012, PR China

¹⁰ Stockholm Observatory, AlbaNova University Center, Stockholms Center for Physics, Astronomy and Biotechnology, Roslagstullsbacken 21, 10691 Stockholm, Sweden

¹¹ Department of Physics, University of Calicut, Kerala 673635, India

¹² IASF-INAF - via Bassini 15, I-20133, Milano, Italy

Received ; accepted

ABSTRACT

Nearly half the stellar mass of present-day spiral galaxies has formed since $z = 1$, and galaxy kinematics is an ideal tool to identify the underlying mechanisms responsible for the galaxy mass assembly since that epoch. Here, we present the first results of the ESO large program, “IMAGES”, which aims at obtaining robust measurements of the kinematics of distant galaxies using the multi-IFU mode of GIRAFFE on the VLT. 3D spectroscopy is essential to robustly measure the often distorted kinematics of distant galaxies (e.g., Flores et al. 2006). We derive the velocity fields and σ -maps of 36 galaxies at $0.4 < z < 0.75$ from the kinematics of the [OII] emission line doublet, and generate a robust technique to identify the nature of the velocity fields based on the pixels of the highest signal-to-noise ratios (S/N). Combining these observations with those of Flores et al., we have gathered a unique sample of 63 velocity fields of emission line galaxies ($W_0([\text{OII}]) \geq 15 \text{ \AA}$) at $z = 0.4 - 0.75$, which are a representative subsample of the population of $M_{\text{stellar}} \geq 1.5 \times 10^{10} M_{\odot}$ emission line galaxies in this redshift range, and are largely unaffected by cosmic variance. Taking into account all galaxies -with or without emission lines- in that redshift range, we find that at least $41 \pm 7\%$ of them have anomalous kinematics, i.e., they are not dynamically relaxed. This includes $26 \pm 7\%$ of distant galaxies with complex kinematics, i.e., they are not simply pressure or rotationally supported. Our result implies that galaxy kinematics are among the most rapidly evolving properties, because locally, only a few percent of the galaxies in this mass range have complex kinematics. It is well-established that galaxies undergoing a merger have complex large-scale motions and thus are likely responsible for the strong evolution of the galaxy kinematics that we observe.

Key words. Galaxies: formation - Galaxies: evolution - Galaxies: kinematics and dynamics

1. Introduction

The resolved 3D kinematics of distant galaxies are a powerful tracer of the major processes governing star-formation and galaxy evolution in the early universe such as merging, accretion, and hydrodynamic feedback related to star-formation and active galactic nucleus (e.g., Barnes & Hernquist 1996; Barton et al. 2000; Dressler 2004). Thus, robustly measuring the internal kinematics of galaxies in the distant universe plays a crucial role for our growing understanding of how galaxies formed and evolved.

Over the last decade, great efforts have been made to study the properties of galaxies in the distant universe (at $z \sim 1$), reveal-

ing a strong evolution with cosmic time. For instance, the cosmic star formation rate (SFR) has declined by a factor ~ 10 from $z \sim 1$ to the present (Lilly et al. 1996; Madau et al. 1996; Hammer et al. 1997; Cowie et al. 1999; Flores et al. 1999). Such a strong evolution of cosmic SFR is consolidated by subsequent works, e.g., Haarsma et al. (2000), Wilson et al. (2002). Although the conclusions are made from different data, they are consistent within a factor of 3 (Hopkins 2004). Heavens et al. (2004) suggest that the cosmic SFR may have reached its peak as late as $z \sim 0.6$. Overall, about half of the stellar mass in intermediate-mass galaxies was formed since $z = 1$, mostly in luminous infrared galaxies (Hammer et al. 2005).

Galaxy interactions and merging may be mechanisms that played a significantly larger role for star-formation in the distant universe than today. Le Fèvre et al. (2000) found that the merger rate in the distant universe was about a factor of 10 times higher

Send offprint requests to: yanbin.yang@obspm.fr

* Intermediate MAss Galaxy Evolution Sequence, ESO programs 174.B-0328(A), 174.B-0328(A), 174.B-0328(E)

than at low redshift (see also Conselice et al. 2003; Bell et al. 2006; Lotz et al. 2006). The high merger rate detected in the distant universe raises a challenge to the standard scenario of disk formation (Hammer et al. 2007). If major mergers generate the ellipticals inevitably, we would find a large fraction of elliptical galaxies rather than about $\sim 70\%$ of spiral galaxies among the intermediate-mass galaxies in the local universe. Similarly, the fraction of luminous compact blue galaxies (LCBGs) increases with redshift by about an order of magnitude out to $z \sim 1$ (Werk et al. 2004; Rawat et al. 2007). LCBGs may be the progenitors of local spheroidal or irregular galaxies at low redshift (e.g., Koo et al. 1995; Guzman 1999), or of the bulges of massive spirals (Hammer et al. 2001; Noeske et al. 2006). 3D spectroscopy of the internal kinematics of LCBGs suggests that they are likely merger remnants (Östlin et al. 2001; Puech et al. 2006a).

Strong evolution as a function of cosmic time has also been claimed for the Tully-Fisher relationship (TFR, Tully & Fisher 1977; Giovanelli et al. 1997), which relates the luminosity and the rotation velocity of disk galaxies. Out to $z \sim 1$, the B-band TFR has been found to have evolved by ~ 0.2 – 2 mag (e.g., Portinari & Sommer-Larsen 2007 and references therein). This brightening of the B-band TFR can be explained by the enhanced star-formation rates at higher redshifts (Ferreras & Silk 2001; Ferreras et al. 2004), but is still a matter of debate. Conselice et al. (2005) do not find significant evolution in either the stellar mass or K-band TFR’s slope or zero point. However, the most striking evolution of the TFR is provided by its large scatter at high redshifts (Conselice et al. 2005), which may be related to the disturbed kinematics of distant galaxies (e.g., Kannappan & Barton 2004).

The rapid time decrease of cosmic SFR, the role of merging in the early evolution of galaxies, and the possible evolution of the TFR are only examples of why measuring the kinematics of distant galaxies precisely and robustly is a *sine qua non* for studying galaxy evolution. However, this is often beyond what can be achieved with classical long-slit spectroscopy. The morphologies and kinematics of distant galaxies are often complex, and their small sizes make it very difficult to precisely position and align the slit. Both limitations can be overcome with integral-field spectroscopy, although the method is relatively complex and time-consuming.

Flores et al. (2006) presented the first study of a statistically meaningful sample of 35 intermediate-mass galaxies at $z=0.4$ – 0.7 , using the integral-field multi-object spectrograph GIRAFFE on the ESO-VLT. They defined a classification scheme to distinguish between rotation and kinematic perturbances, which may stem from interactions and mergers, from the 3D kinematics and high-resolution HST imaging. Intriguingly, they find that the large scatter of distant TFR shown in previous studies is due to non-relaxed systems while the pure rotational disks exhibit a TFR that is similarly tight as that of local spirals. Here, we present another sample of 36 galaxies with very similar selection criteria, to enlarge the total sample size and put the conclusions on statistically more robust grounds. This is the first of a series of publications related to the ESO-VLT large program IMAGES, which aims at studying the evolutionary sequence of galaxies over the last 8 Gyrs (see Ravikumar et al. 2007 for more details).

The paper is organized as follows. In Sect. 2 we describe the observations and the sample selection. The methodology to describe and classify the distant galaxy kinematics is shown in Sect. 3, as well as a detailed description of the 36 observed velocity fields (VFs). Sections 4 and 5 include the discussion and the conclusion. In this paper, we adopt the Concordance cos-

Table 1. Journal of observations.

Run ID	Setup	Exposure (hr)
174.B-0328(A)	L04	10
073.A-0209(A)	L05	4.5
174.B-0328(A)	L05	10.6
174.B-0328(E)	L05	10.4

mological parameters of $H_0 = 70 \text{ km s}^{-1} \text{ Mpc}^{-1}$, $\Omega_M = 0.3$ and $\Omega_\Lambda = 0.7$.

2. Data

2.1. Observations

We used the FLAMES-GIRAFFE multi-object integral-field spectrograph on the ESO-VLT in the multi-IFU mode to measure the velocity and dispersion fields of a statistically meaningful sample of galaxies at redshifts $z = 0.4$ – 0.75 from their $[\text{OII}]\lambda 3726, 3729$ emission. Each integral-field unit (IFU) of GIRAFFE consists in 20 micro-lenses with $0.52''$ spatial sampling, resulting in a $2'' \times 3''$ field of view per IFU. We used the LR04 and LR05 set-ups, which correspond to spectral resolutions of 0.55 \AA (30 km s^{-1}) and 0.45 \AA (22 km s^{-1}), respectively.

Observations were carried out as part of the IMAGES large program, complemented by guaranteed time observations (programs 174.B-0328(A), 073.A-0209(A), 174.B-0328(A), 174.B-0328(E), see also Table 1). The total observing time was 5 nights, with integration times ranging from 4.5 to 15 hrs for individual targets. The seeing ranged from $0.4''$ to $1''$, with a median value of $0.8''$. Data reduction and the construction of the final data cubes are described in detail in Flores et al. (2006).

2.2. Sample selection

Our targets are a subset of the Chandra Deep Field South, with redshifts $z \sim 0.4$ – 0.75 , $I_{\text{AB}} \leq 23.5$ and detected $[\text{OII}]\lambda 3726, 3729$ emission lines ($W_0([\text{OII}]) \geq 15 \text{ \AA}$, Ravikumar et al. 2007). Our goal is to investigate a sample of intermediate mass galaxies (see Hammer et al. 2005), therefore we required J -band absolute magnitudes brighter than $M_J(\text{AB}) = -20.3$. Such a limit corresponds approximately to a stellar mass of $M_{\text{stellar}} \geq 1.5 \times 10^{10} M_\odot$ when converting the J -band luminosity using the prescription discussed in Bell et al. (2003; see also Hammer et al. 2005). Ravikumar et al. (2007) has convincingly shown that within the redshift range of 0.4 – 0.75 , $I_{\text{AB}} \leq 23.5$ galaxies include almost all intermediate mass galaxies (e.g., at least 95% of $M_J(\text{AB}) \leq -20.3$ galaxies, see their Sect. 3.4). Given all the above, our sample comprises a total of 46 targets. The relatively small number of suitable galaxies and small bandpass of the GIRAFFE set-ups make it difficult to fill all 15 IFUs with galaxies with spectroscopic redshifts. We therefore used empty “bonus” IFUs to observe galaxies for which only photometric redshifts were known, but could not detect any because of the large uncertainties of photometric redshifts.

Moreover, we rejected 2 galaxies with spurious features that were identified as $[\text{OII}]$ emission lines in their spectra (J033221.42-274231.2, J033241.08-274853.0), 4 targets due to faint line emission (i.e., $W_0([\text{OII}]) < 15 \text{ \AA}$: J033211.41-274650.0, J033226.00-274150.6, J033232.13-275105.5, J033254.50-274703.6), and one due to the CCD defects (J033213.85-274248.9). Another 2 galaxies (J033212.36-274835.6, J033236.72-274406.4) were rejected by our mini-

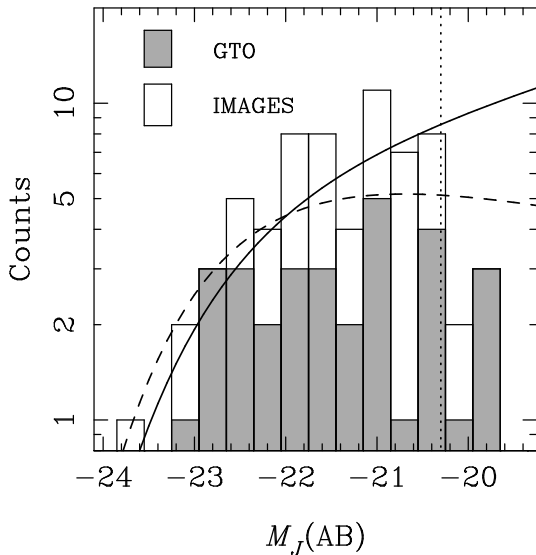


Fig. 1. Number counts (in logarithmic scale) of selected galaxies versus AB absolute magnitude in J -band. The GTO sample refers to Flores et al. (2006); the IMAGES sample refers to this paper. The vertical dotted line indicates the limit of the IMAGES program. Two luminosity functions derived from Pozzetti et al. (2003) are shown (full line: $z = 0.5$; dashed line: $z = 1$). The galaxies of our sample have redshifts ranging from $z = 0.4$ to $z = 0.75$. This implies that the combined sample of 63 galaxies with $M_J(\text{AB}) \leq -20.3$ is representative of galaxies with stellar masses larger than $1.5 \times 10^{10} M_{\odot}$ at $z \sim 0.6$.

imum quality criterion: at least 4 GIRAFFE spatial pixels with spectral $S/N > 4$. The galaxy J033229.71-274507.2 was also rejected because emission was detected in only 4 GIRAFFE pixels, which is not sufficient to classify its kinematics. Finally, we obtained a sample of 36 well resolved galaxies of intermediate stellar mass with good S/N values.

2.3. Representativeness/completeness of the sample

Figure 2.3 shows the distribution of the J -band absolute magnitudes (also listed in Table 2) for the sample studied in this paper, combined with the Flores et al. (2006) sample of 35 galaxies. Both samples can be merged because the selection of Flores et al. is very similar to that of this paper and because both studies used essentially the same instrumental set-ups. Applying our criteria of $M_J(\text{AB}) \leq -20.3$ and $W_0([\text{OII}]) \geq 15 \text{ \AA}$, we are left with 63 galaxies with data of appropriate quality to carry out our analysis. We compared the luminosity distribution of the sample to the luminosity function at redshift of 0.5 and 1 (Fig. 2.3). Kolmogorov-Smirnov tests support that our sample follows the luminosity function in the $z = 0.4-0.75$ range at $> 99.9\%$ confidence level. Furthermore, the combined two samples include galaxies from 4 different fields, namely the CDFS, HDF5, CFR503h and CFR522h. It is then unlikely that our conclusions are strongly affected by statistical effects, possibly related to large scale structures (see Sect. 4 for more analysis, also Ravikumar et al. 2007). Our sample is a completely representative sub-sample of $M_J(\text{AB}) \leq -20.3$ emission line selected galaxies at $z = 0.4-0.75$. To our knowledge, it is the only such existing sample of distant galaxies with measured 3D kinematics.

3. Kinematics of distant galaxies

3.1. Measuring galaxy kinematics using the $[\text{OII}]$ doublet

Our method to extract kinematic fields from 3D spectroscopy of the $[\text{OII}]\lambda 3737, 3729$ emission line doublet has been described in detail in Flores et al. (2006). Here, we only give a brief overview, and highlight recent improvements. The 20 individual spectra of each object were inspected visually to detect possible artefacts or contamination with night sky lines. We then constructed the 3D data cube around the expected observed $[\text{OII}]$ wavelength with and without sky subtraction, and fitted the $[\text{OII}]$ doublet with two Gaussian, keeping the wavelength difference between the two lines at rest-frame $\lambda_2 - \lambda_1 = 2.783 \text{ \AA}$ fixed, and requiring that both lines have the same dispersion, $\sigma_1 = \sigma_2$. The line ratio is a free parameter except when the fit failed, in which case we impose a ratio of $R(3729/3727) = 1.4$, which corresponds to the low density limit and is appropriate for most galaxies (see also Puech et al. 2006b; Weiner et al. 2006).

We estimate the systemic velocity of each galaxy from the σ -clipped mean of the spatially-resolved velocities, and measure the width of night sky lines to correct the dispersion maps (σ -maps) for instrumental resolution. We also derive S/N -maps to quantify the uncertainty of the kinematics following the definition of Flores et al. (2006); in particular, we use only those spectra where the $[\text{OII}]$ line emission is detected with a $S/N \geq 3$, and apply a simple 5×5 linear interpolation to the VF and σ -map. We show the VF, σ -maps and S/N -maps in Fig. 2 with the high resolution ($0.03''/\text{pixel}$) ACS F775W image for each object. The analysis of the full sample was done independently by several of us (HF, BN, MP and YY), before comparing and finalizing the results.

Since Flores et al. (2006), we have improved our analysis software to better account for the contamination of the emission line spectrum with night sky lines, fitting the $[\text{OII}]$ emission lines and superimposed night sky lines simultaneously. This is particularly relevant with the L05 set-up ($5741 - 6524 \text{ \AA}$), where the risk of overlaps is important due to a relatively large number of night sky lines. At the relatively high effective resolving power of GIRAFFE of $R \geq 10000$, the $[\text{OII}]$ emission lines are significantly broader than the night sky lines, which is essential to successfully isolate the signal (see Fig. 3 for an example). By fitting the sky and object simultaneously, we have been able to recover the kinematics of 3 galaxies that were particularly strongly blended with night sky lines, and would have been otherwise rejected (J033217.62-274257.4, J033220.48-275143.9, J033244.20-274733.5).

3.2. Classification of the kinematics of distant galaxies

Flores et al. (2006) developed a simple kinematic classification scheme for distant galaxies based on their 3D kinematics and their morphology in the ACS F775W images. It relies on the fact that at low spatial resolution, a rotating disk should show a well defined peak in the center of the σ -map, which corresponds to the convolution of the large scale motion (i.e., the rotation) with the (relatively small) dispersion of the gas in the disk or in the bulge. Indeed, the central parts of the galaxy, where the rotation curve rises most quickly, are not spatially resolved with ground-based optical spectroscopy and our classification fully accounts for its convolution with the actual PSF (point spread function). To summarize, we distinguish between the following classes :

1. **Rotating disks (RD):** the VF shows an ordered gradient, and the dynamical major axis is aligned with the morphological

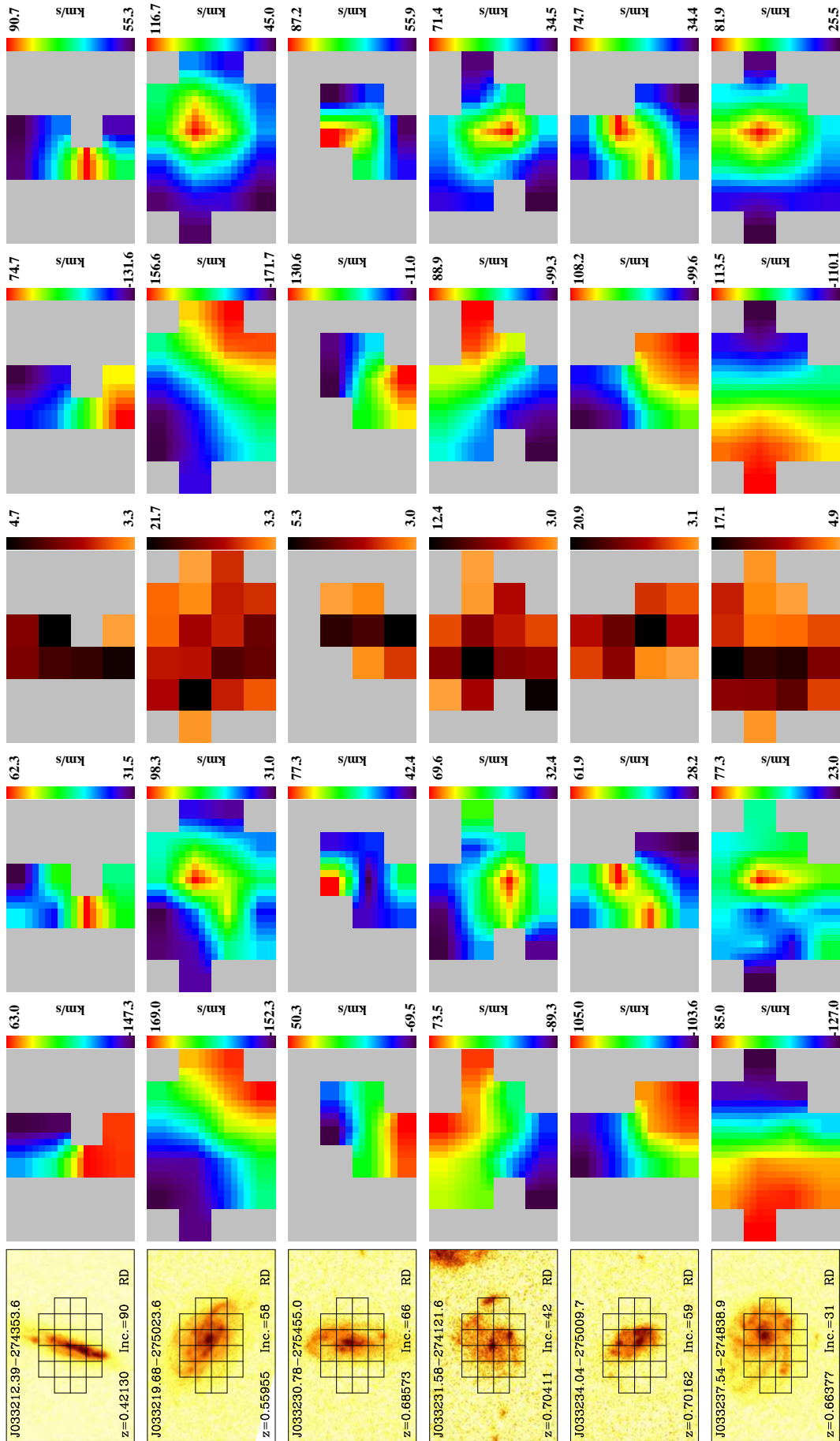


Fig. 2. Kinematics of the individual galaxies. Each row corresponds to one galaxy. From left to right, we show the HST/ACS F775W images, the observed VFs, σ -maps and S/N-maps, the model VFs and σ -maps. A grid of GIRAFFE IFU superposed on the HST image indicates the position and the scale of IFU with respect to the galaxy. We have applied a 5×5 linear interpolation to the VFs and σ -maps for visualization.

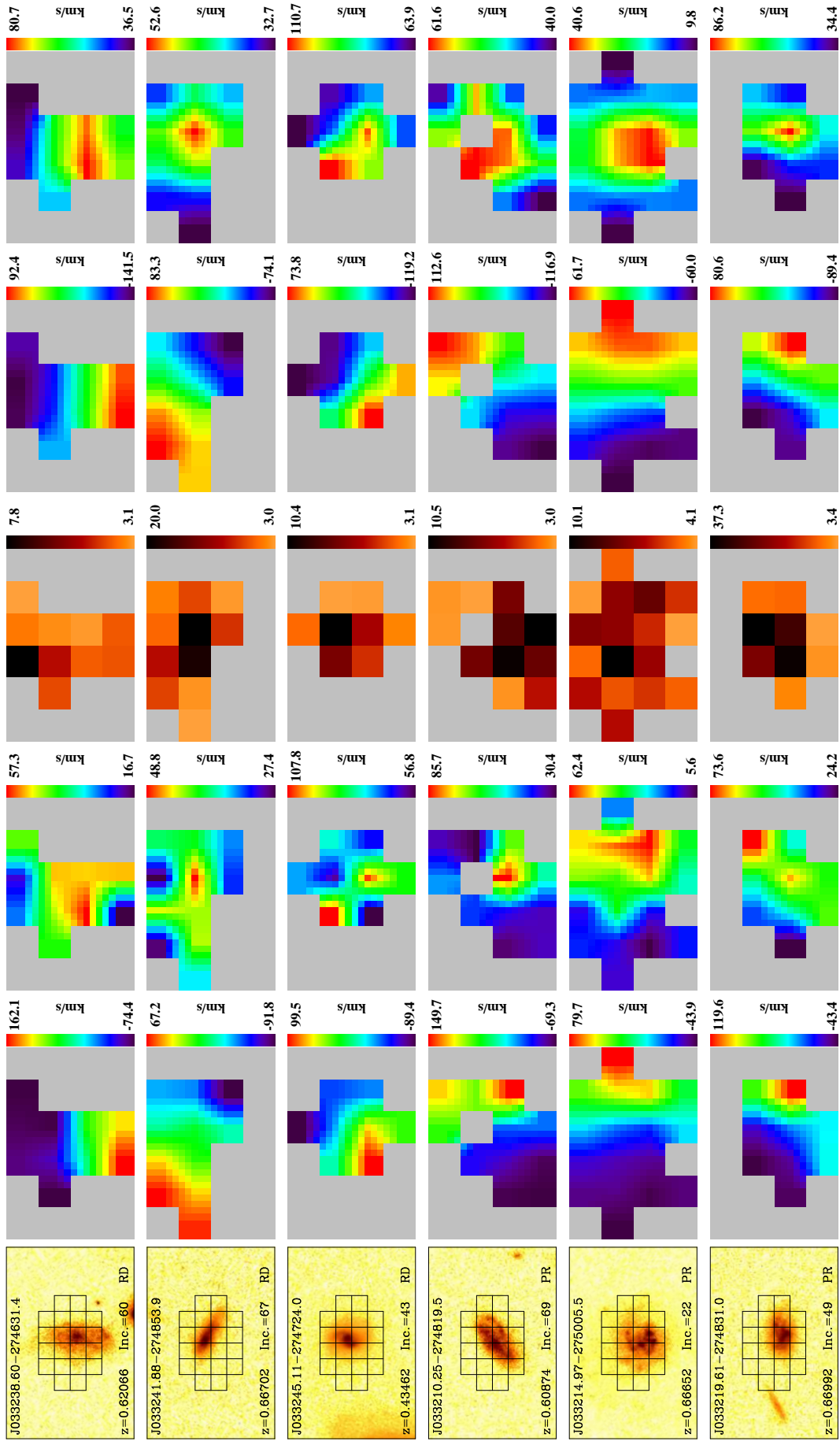


Fig. 2. continued.

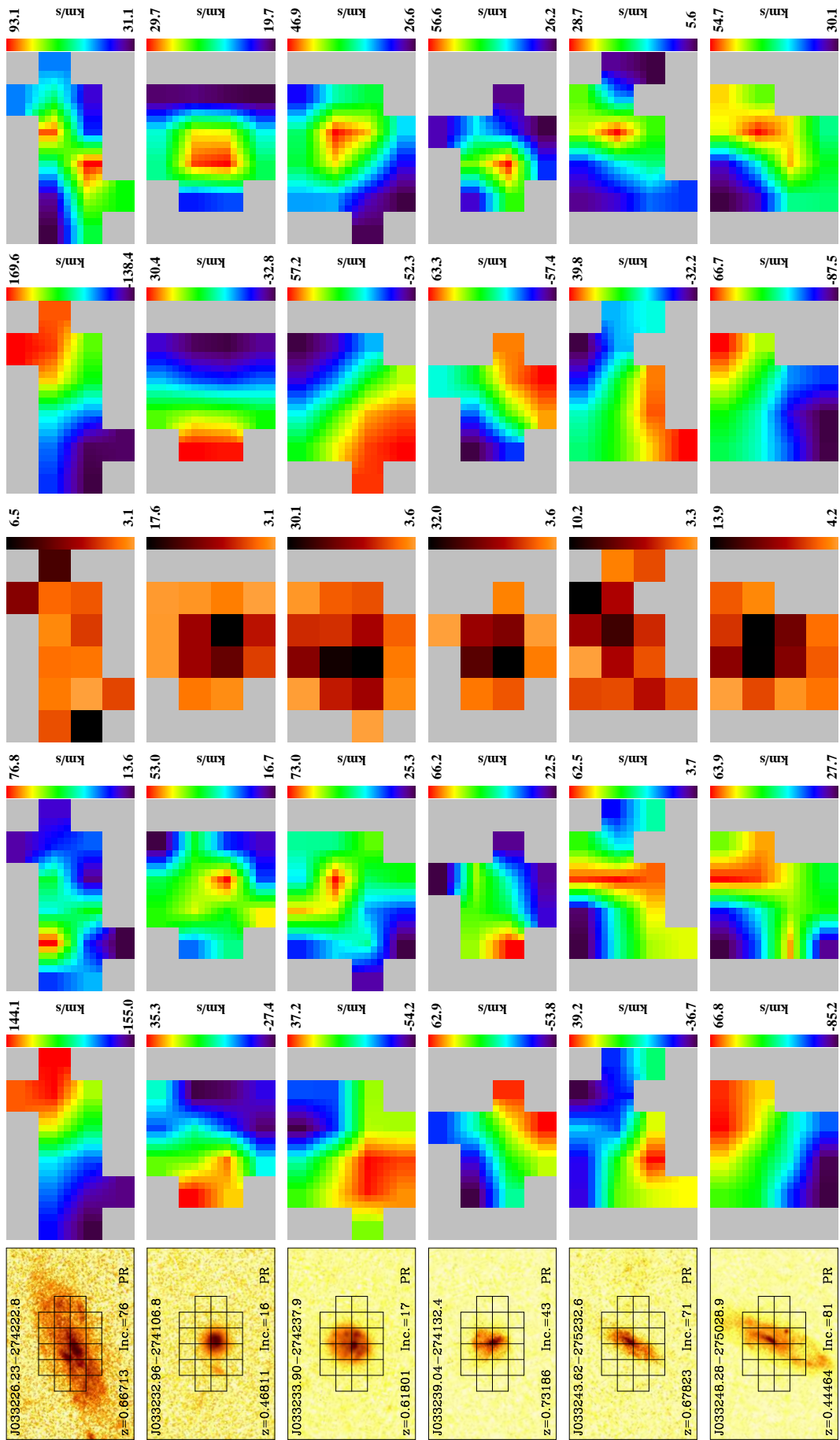


Fig. 2. continued.

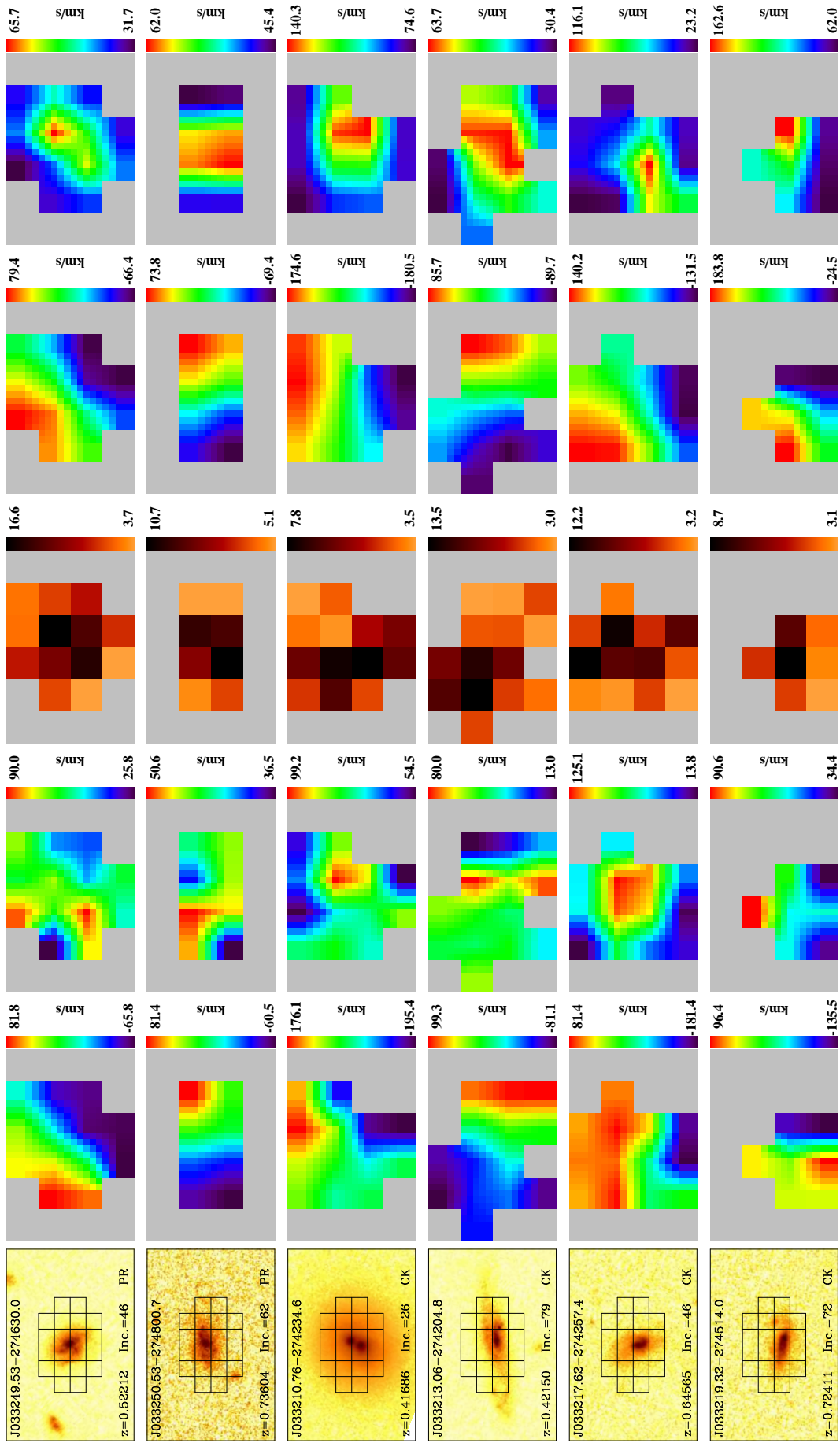


Fig. 2. continued.

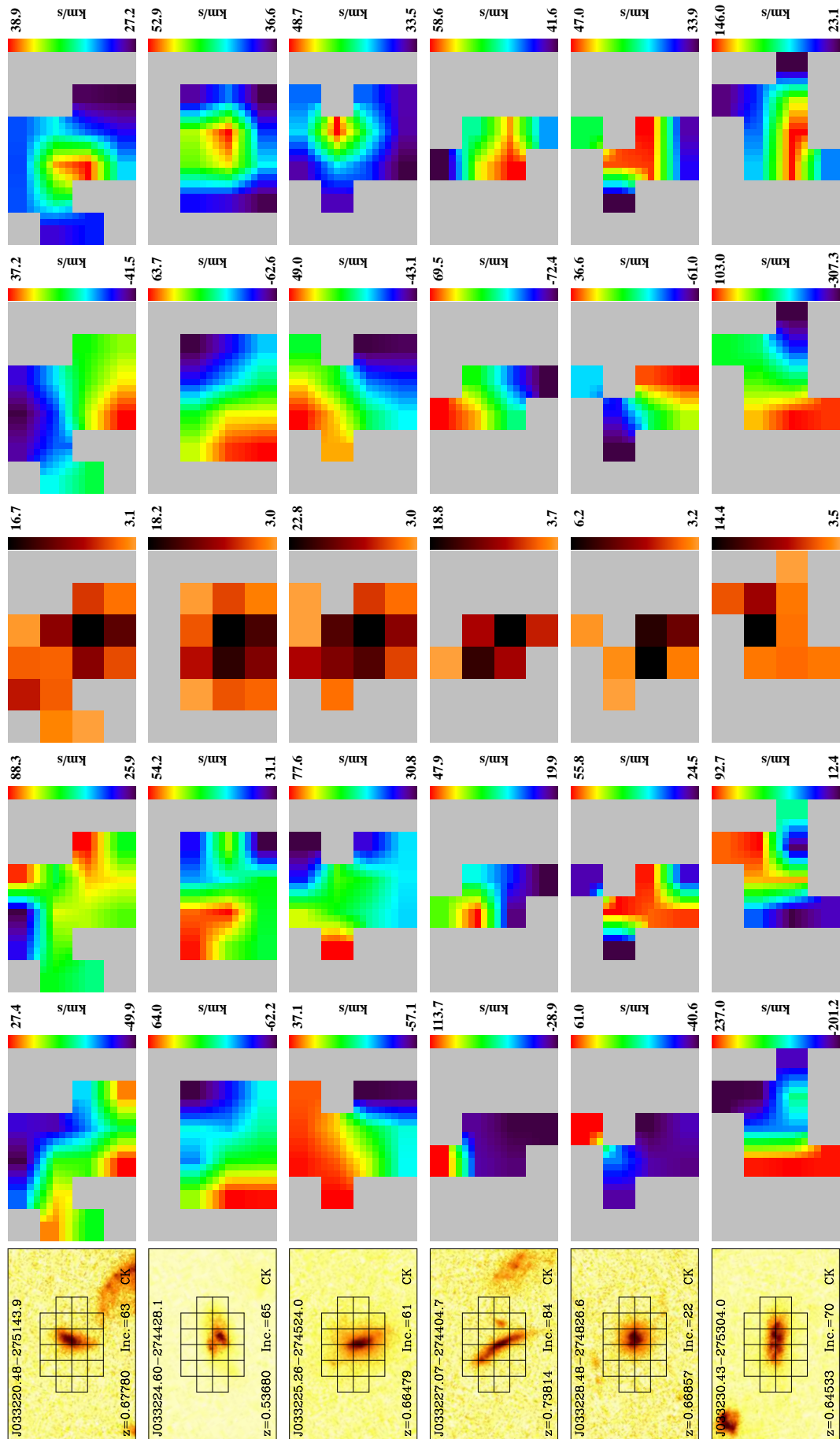


Fig. 2. continued.

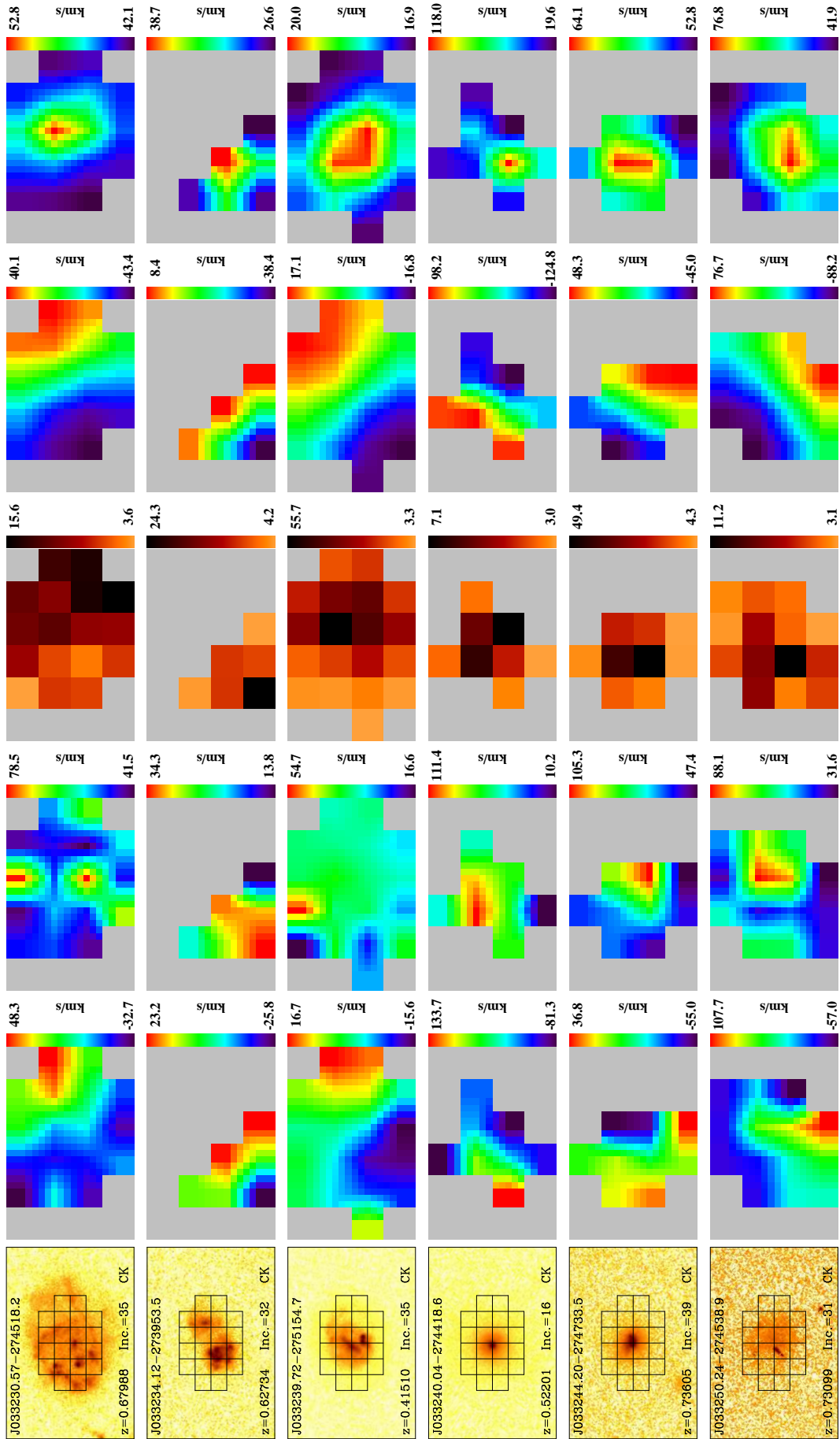


Fig. 2. continued.

Table 2. Properties of the 39 galaxies of the IMAGES sample.

GOODS ID	RA & DEC (J2000.0)	z^a	M_B^b	M_J^b	$i^{c,e}$	C ^d	Δi^e	ϵ^e
J033212.39-274353.6	03:32:12.387 -27:43:53.59	0.42130	-19.55	-21.58	90.0(5.0)	RD	0.08(0.32)	0.13(0.03)
J033219.68-275023.6	03:32:19.678 -27:50:23.57	0.55955	-20.88	-22.37	58.3(6.7)	RD	0.11(0.46)	0.06(0.01)
J033230.78-275455.0	03:32:30.780 -27:54:54.99	0.68573	-20.51	-21.90	66.1(4.3)	RD	0.11(0.31)	0.12(0.02)
J033231.58-274121.6	03:32:31.575 -27:41:21.63	0.70411	-20.16	-20.69	42.2(9.6)	RD	0.11(0.57)	0.01(<.01)
J033234.04-275009.7	03:32:34.037 -27:50:09.69	0.70162	-19.88	-20.61	59.3(3.4)	RD	0.09(0.21)	0.17(0.02)
J033237.54-274838.9	03:32:37.538 -27:48:38.94	0.66377	-21.29	-22.07	30.7(12.)	RD	0.11(0.35)	0.04(0.01)
J033238.60-274631.4	03:32:38.595 -27:46:31.37	0.62066	-20.03	-21.54	60.2(4.3)	RD	0.16(0.34)	0.08(0.02)
J033241.88-274853.9	03:32:41.883 -27:48:53.86	0.66702	-20.32	-21.00	66.5(6.2)	RD	0.03(0.50)	0.08(0.01)
J033245.11-274724.0	03:32:45.108 -27:47:24.00	0.43462	-20.13	-22.06	43.3(6.2)	RD	0.14(0.18)	0.09(0.02)
J033210.25-274819.5	03:32:10.250 -27:48:19.49	0.60874	-19.76	-20.93	68.5(4.5)	PR	0.83(0.19)	0.40(0.07)
J033214.97-275005.5	03:32:14.971 -27:50:05.45	0.66652	-21.50	-22.53	21.9(8.2)	PR	1.32(0.27)	0.65(0.12)
J033219.61-274831.0	03:32:19.606 -27:48:30.97	0.66992	-20.36	-20.99	49.1(7.0)	PR	0.40(0.35)	0.18(0.01)
J033226.23-274222.8	03:32:26.229 -27:42:22.81	0.66713	-20.71	-22.01	76.4(3.1)	PR	0.72(0.42)	0.40(0.09)
J033232.96-274106.8	03:32:32.959 -27:41:06.78	0.46811	-19.50	-20.45	16.0(3.8)	PR	0.64(0.37)	1.15(0.14)
J033233.90-274237.9	03:32:33.897 -27:42:37.93	0.61801	-20.99	-21.91	17.2(10.)	PR	0.07(0.26)	1.35(0.17)
J033239.04-274132.4	03:32:39.044 -27:41:32.43	0.73186	-20.46	-20.75	43.2(10.)	PR	0.44(0.25)	0.24(0.01)
J033243.62-275232.6	03:32:43.623 -27:52:32.63	0.67823	-19.27	-20.03	70.8(1.6)	PR	0.15(0.63)	1.54(0.25)
J033248.28-275028.9	03:32:48.281 -27:50:28.88	0.44464	-19.35	-20.47	80.8(3.3)	PR	0.34(0.82)	0.40(0.04)
J033249.53-274630.0	03:32:49.525 -27:46:29.98	0.52212	-20.05	-21.09	45.6(2.2)	PR	1.10(0.58)	0.38(0.03)
J033250.53-274800.7	03:32:50.534 -27:48:00.67	0.73604	-19.99	-20.50	62.3(3.9)	PR	0.22(0.62)	0.30(0.04)
J033210.76-274234.6	03:32:10.761 -27:42:34.58	0.41686	-21.78	-23.70	26.0(7.4)	CK	0.74(0.54)	0.47(0.09)
J033213.06-274204.8	03:32:13.061 -27:42:04.81	0.42150	-19.53	-20.67	78.7(2.8)	CK	0.68(0.30)	0.02(<.01)
J033217.62-274257.4	03:32:17.620 -27:42:57.44	0.64565	-19.78	-21.23	46.3(8.4)	CK	1.07(0.21)	0.04(0.01)
J033219.32-274514.0	03:32:19.317 -27:45:14.04	0.72411	-20.31	-21.24	72.1(4.5)	CK	0.15(0.17)	0.66(0.12)
J033220.48-275143.9	03:32:20.484 -27:51:43.93	0.67780	-19.93	-20.72	63.4(3.6)	CK	1.05(0.30)	2.94(0.42)
J033224.60-274428.1	03:32:24.601 -27:44:28.12	0.53680	-19.58	-20.44	64.8(1.2)	CK	0.99(0.48)	0.42(0.04)
J033225.26-274524.0	03:32:25.260 -27:45:23.97	0.66479	-20.90	-21.63	60.5(6.0)	CK	0.87(0.19)	1.00(0.09)
J033227.07-274404.7	03:32:27.074 -27:44:04.66	0.73814	-20.34	-21.04	84.2(1.7)	CK	0.69(0.14)	0.91(0.13)
J033228.48-274826.6	03:32:28.477 -27:48:26.55	0.66857	-20.10	-21.74	22.4(5.0)	CK	0.67(0.24)	1.35(0.26)
J033230.43-275304.0	03:32:30.429 -27:53:04.02	0.64533	-19.96	-21.71	70.3(2.4)	CK	1.02(0.24)	0.44(0.09)
J033230.57-274518.2	03:32:30.569 -27:45:18.24	0.67988	-21.93	-22.95	34.5(9.4)	CK	1.04(0.52)	0.16(0.02)
J033234.12-273953.5	03:32:34.120 -27:39:53.53	0.62734	-23.08	99.99	32.1(4.5)	CK	0.12(0.18)	0.53(0.08)
J033239.72-275154.7	03:32:39.719 -27:51:54.68	0.41510	-20.10	-21.04	35.4(1.3)	CK	1.55(0.45)	5.15(0.26)
J033240.04-274418.6	03:32:40.040 -27:44:18.63	0.52201	-20.55	-22.04	15.6(11.)	CK	0.37(0.22)	0.36(0.08)
J033244.20-274733.5	03:32:44.199 -27:47:33.48	0.73605	-21.08	-21.86	39.0(5.8)	CK	0.64(0.15)	0.62(0.03)
J033250.24-274538.9	03:32:50.239 -27:45:38.92	0.73099	-19.79	-20.70	31.3(8.8)	CK	1.37(0.38)	0.59(0.08)
J033212.36-274835.6	03:32:12.360 -27:48:35.64	0.56210	-20.13	-21.16	65.8(1.4)	UC	-	-
J033229.71-274507.2	03:32:29.707 -27:45:07.20	0.73170	-20.05	-20.88	42.3(6.2)	UC	-	-
J033236.72-274406.4	03:32:36.715 -27:44:6.435	0.66500	-20.23	-22.01	58.7(1.8)	UC	-	-

^a Redshift measured by [OII] emission.

^b Absolute magnitudes in B - and J - band.

^c Inclination of galaxies and its error (in unit of degree).

^d Kinematical classification (see Sect. 3.2 for details): RD-rotating disks; PR-perturbed rotations; CK-complex kinematics; UC-unclassified.

^e The corresponding error of each quantity is given into brackets.

major axis. The σ -map indicates a single peak close to the dynamical center;

2. **Perturbed rotations (PR):** the kinematics shows all the features of a rotating disk (see above), but the peak in the σ -map is either absent or clearly shifted away from the dynamical center;
3. **Complex kinematics (CK):** neither the VF nor the σ -map are compatible with regular disk rotation, including VFs that are misaligned with the morphological major axis.

According to these definitions of 3 kinematical classes, we have classified the 36 galaxies of our sample. To do so, each galaxy has been examined by 5 of us (HF, FH, BN, MP and YY), before comparing our classification. The results are listed in Table 2, which also includes absolute magnitudes and inclinations. Absolute magnitudes are derived using the procedure described by Hammer et al. (2005), based on photometry at near

IR and optical wavelengths (see also Ravikumar et al. 2007). Inclinations were measured using ellipsoidal isophotes near the optical radius from HST/ACS F775W and F814W imaging. Comparison between estimates from different team members and with values derived from SExtractor (Bertin et al. 1996) suggests that typical uncertainties are about 5° .

In some cases, classification is not an easy task. There are two galaxies (J033234.04-275009.7, J033245.11-274724.0) that possess double σ -peaks in GIRAFFE IFU view. They are classified to be RD because the center of the galaxy is just located in between the two adjacent GIRAFFE IFU pixels. These phenomena have been reproduced in our model (see Fig. 2). However, another galaxy J033219.61-274831.0, which is classified as PR, has its two σ -peaks located at one side of the galaxy center, which is not expected from a rotating disk.

In the next paragraphs, we will describe quantitatively the differences between kinematical classes, a test of the robustness

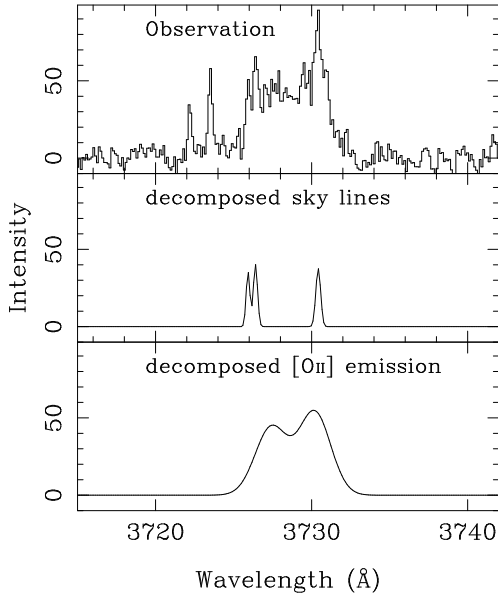


Fig. 3. Example of a simultaneous fit to the emission line of a galaxy with superimposed night sky lines. The top panel shows the observed [OII] emission, which has three night sky lines superimposed. The mid panel shows the isolated components of the night sky lines after the fit, and the bottom panel shows the reconstructed [OII] emission line doublet.

of our classification scheme and a description of each individual target.

3.3. A powerful diagnostic of the classification

3.3.1. Measuring the discrepancy from a pure rotational disk

Flores et al. (2006) developed a diagnostic method to test the validity of the classification, and to quantify the deviation of a given VF from that of a pure rotational disk. First, we identify the VF, based on the largest scale motion in each galaxy. We then assume that this VF is the result of pure rotational motion, whatever the true nature of the dynamics. We then model the VF of a rotating disk that matches the observed velocity gradient estimated from the measured minimal and maximal velocities to obtain the expected σ -map corresponding to the observed VF (a “model VF”). In particular, we take into account that most of the velocity gradient in the central region (from 45% to 70%) falls within one spatial pixel of GIRAFFE, as we observe in well-identified rotating disks. To generate the model VF and σ -map shown in Fig. 2, we then use a single rotation curve that concentrates an equivalent fraction of the velocity gradient in one GIRAFFE pixel. While this should not affect the location of the σ peak, we are aware that this simplistic assumption may affect the σ peak intensity for some galaxies with flatter rotation curves or with a prominent bulge. Finally, for model σ -map, we assume that the intrinsic dispersion (due to the random gas motion in the disk) is the smallest dispersion observed in the data.

The model VF for each galaxy has then been generated by assuming a rotation curve that is been used to generate a model data cube. Note that, whenever possible, we tried to align the model rotational axis with the major axis of the galaxy, in agreement with the rotating disk hypothesis. Unlike what was done in Flores et al. (2006), we do not try to correct for inclination, as the observed and the model VFs are affected in a similar way by inclination effects. However, note that the inclination is used

during the process to define the geometrical extent of the VF in the plane of the sky, assuming a thin disk. Further, we compute the corresponding IFU σ -map by considering the effects of seeing. By comparing the observed and model σ -maps, we can estimate whether the observed kinematics are consistent or not with a rotating disk.

Two parameters are then computed to characterize the differences between the two σ -maps, taking the model σ -map as a reference. The first parameter is the spatial separation (Δr , in GIRAFFE pixels) between the peaks in the two σ -maps. This indicates how the center of rotation is recovered by our observation. For each σ -map the pixel including the σ peak is identified, and then the peak location is calculated as the barycenter of the surrounding pixels. We verify that weighting the barycenter by S/N does not change the result, so we choose a uniform weight for each pixel. The second parameter is the relative difference (ϵ) between the amplitudes of the modeled and observed σ peaks. We define ϵ as:

$$\epsilon = \frac{|\sigma_{\text{obs}} - \sigma_{\text{mod}}|}{\sigma_{\text{mod}}} \Big|_{\text{location of the peak of model } \sigma\text{-map}}. \quad (1)$$

This definition significantly improves the robustness of the test compared with what was done in Flores et al. (2006), because the test is now applicable to the pixels of highest S/N in the center of the σ -map. One may wonder whether the test is reliable, given the possible uncertainties due to our observational set-up with low spatial resolution and limited S/N, especially in the outskirts of the galaxies. In fact, some parts of the VF of distant galaxies might have been missed, for example, when the galaxy may extend further than the IFU. Alternatively, low S/N near our cut-off limit may generate an absence of detection in some extended parts of the galaxy. An illustration of this is given by J033230.78-275455.0 (see Fig. 2), for which the S/N ratio is below the cut-off for almost half the disk. This means that for some objects we may have missed part of the rotation curve, or we may have introduced an artificial asymmetry. The immediate consequence of this would be to generate a σ peak that is smaller in amplitude than the real one and/or that is slightly offset from the rotational center. However, the impact of the above has to be quite marginal and has no effect on our classification after a careful examination of individual VFs. Moreover, with our method to build model rotational VFs, the maximal model rotation is produced by the observed large scale motions, and we do use the same hot pixels for both model and observed maps.

Figure 4 shows the diagnostic diagram of Δr versus ϵ . We have recalculated ϵ for the 32 classified galaxies from Flores et al. 2006, and plotted them in the same figure. While modifying the definition clearly changes the location of the points, we confirm all the results of Flores et al., i.e., that rotating disks have locations near $\Delta r \sim \epsilon \sim 0$, while galaxies with anomalous VFs are clearly offset. **We have performed simulations of two local interacting pairs: ARP 271 and KPG 468 (Fuentes-Carrera et al. 2004; Hernández-Toledo et al. 2003), which are supposed to be CK systems. We assume that they are located at $z=0.6$ and observed by GIRAFFE IFU mode in the simulations. Following our method, we find these two simulated CKs (indicated by black crosses) are located far from the rotating disks, supporting our diagnostic method.**

3.3.2. Using χ^2 -test to recognize disk kinematics

Given the spatial resolution of IFU and the seeing during observations, we only have a few degrees of freedom to confine

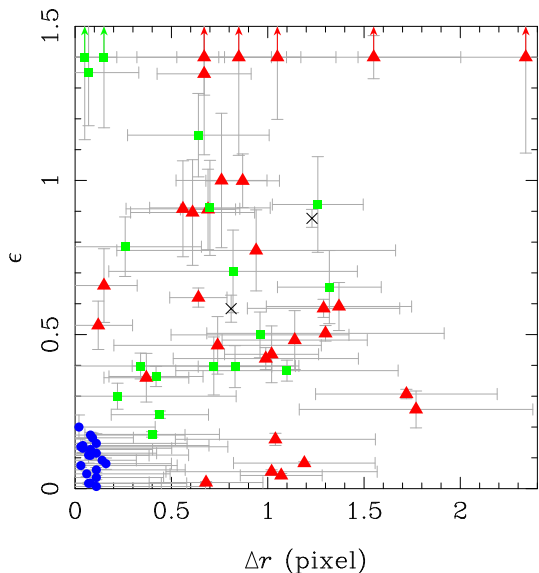


Fig. 4. Diagnostic diagram of the galaxy kinematics. Δr is the spatial separation between the peaks of the modeled and the observed σ -maps. ϵ gives the relative difference between the velocity dispersions of the model and the observation at the reference location of the peak of the model σ -map. The blue dots, green squares and red triangles represent the RD, PR and CK galaxies, respectively. Typical uncertainties are 0.3 spatial pixels in Δr , and 15% in ϵ . (see Sect. 3.3 for more details.)

the model. Hence, χ^2 -test may not be an ideal tool for comparing the model and the observations. A series of tests have been performed in order to explore the validity of the χ^2 estimator of goodness of the fits. In Fig. 5 we present a best-fitting χ^2 -diagram for the CDFS sample. First, we fit the observational VF-map with a rotation model, then we calculate the reduced χ^2 which is set as abscissa. The corresponding σ -map is generated following the same method described in the previous section, then the reduced χ^2 for the σ -map is computed and presented as ordinates. The two simulated galaxy pairs, ARP271 and KPG468 (see the caption of Fig. 4 for more details), are also plotted. Although, the CK systems tend to have larger χ^2 than the RD and PR, it is difficult to distinguish different kinematical classes with such diagram.

Taking into account the spatial resolution of the GIRAFFE IFU, the most important features of a rotating disk are (a) a well ordered VF with dynamical axis following the optical major-axis of the galaxy, (b) a clear σ -peak located at the position of the galaxy center, (c) and the σ -peak having a reasonable value, which can be generated by rotation. These important features are somehow diluted by the χ^2 -test as it is presented in Fig. 5. For example, J033230.78-275455.0, a RD galaxy, has a reduced χ^2 close to 1 in both VF- and σ - maps because of its relatively low averaged S/N ($= 4$); other galaxies (which have typically averaged S/N ~ 8) have χ^2 of ~ 10 . The χ^2 -test appears to be too sensitive to the averaged S/N. Furthermore, using this type of test we cannot distinguish whether one of the simulated galaxy pairs (KPG468) is a RD or a PR, since the χ^2 value of this pair is similar to that of both RDs and PRs. Since the χ^2 values are to some extent scaled by the errors that are related to the S/N, we also tried to apply an unweighted χ^2 -test. In this case, we still have the same disordered distribution over the χ^2 diagram.

Consequently, the χ^2 -test seems less efficient than our method (see Sect. 3.3.1 and Fig. 4) in recognizing disk kinematics from perturbed and complex kinematics.

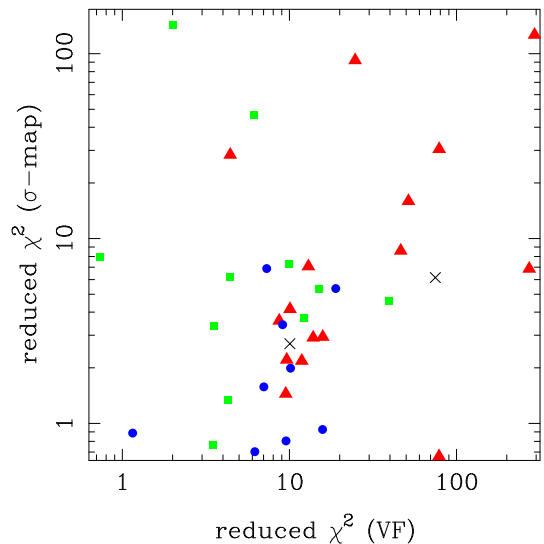


Fig. 5. The χ^2 -diagram for the best-fitting rotation model of galaxy kinematics. The reduced χ^2 for VF-map and σ -map are set to be abscissa and ordinates, respectively. The blue dots, green squares and red triangles represent the RD, PR and CK galaxies, respectively. The two black crosses indicate the two simulated galaxy pairs: ARP271 and KPG468 (see Sect. 3.3.1 for more details). Although the CKs tend to have higher χ^2 than the PRs and the RDs, it is still less efficient to identify different kinematics with this diagram. (see Sect. 3.3.2 for more discussion.)

From perturbed and complex kinematics. Therefore, we choose to compare the observations with the rotating disk model using the methodology developed in Sect. 3.3.1.

3.3.3. Error estimates

We used Monte-Carlo simulations to evaluate the uncertainty of our velocity dispersion measurements. First, we generate $\sim 50\,000$ artificial [OIII] emission line doublets with S/N ranging from 3 to 40. The flux ratio within the doublets is fixed at 1.4. Simulated dispersions range from 10 to 100 km s $^{-1}$, corresponding to the minimum and maximum of our observations, respectively.

In order to remove possible artefacts in the data, we analyzed the spectrum of each spatial pixel manually in each data cube before thoroughly analyzing the spectral fit of each individual line. To ensure that the Monte-Carlo simulations are a fair representation of this process, we did not only consider the results from automatic fitting routines, but use the same procedure that was used for the observed data-cubes. This is particularly important for spectra with low S/N (i.e., 3–5) spectra, and it somewhat reduces the uncertainties of our measurement.

We then investigated the uncertainties in the velocity dispersion as a function of the S/N. Figure 6 shows the relative uncertainty in the velocity dispersion ($\Delta\sigma/\sigma$) as a function of the S/N. **We find a slight trend that we possibly underestimate velocity dispersion when we have spectra with S/N lower than ~ 5 , because the noise affects the line wings in particular. However, this systematic uncertainty is negligible compared to the statistical error.** Based on this result, we estimate the uncertainty of the observed velocity dispersion at a given S/N. Standard error propagation then yields the uncertainty on ϵ (Eq. 1). Typically, we find that uncertainties

are $\sim 15\%$, ranging from 5% to 25% (see Table 2 for the uncertainties of individual objects).

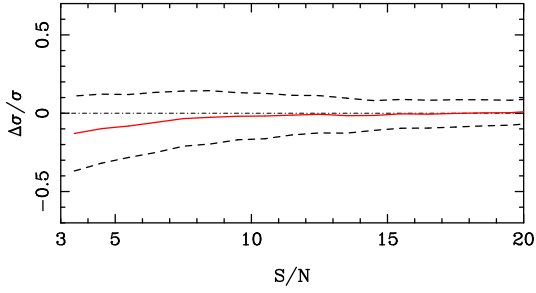


Fig. 6. The red solid line indicates the median differences between the measured and the simulated σ values varying with the S/N. The two dashed lines give the 1σ errors for each bin in S/N: typically, these amount to $\sim 20\%$ at $3 < S/N < 4$, 15% at $S/N \sim 10$ and about 5% at $S/N > 15$, respectively.

Uncertainties in Δr are dominated by the error on the location of the peak of the velocity dispersions. This uncertainty is dominated by the profile of the σ -map and its S/N. Again, we use Monte-Carlo simulations to quantify these uncertainties. We calculate the uncertainty of each value in our σ -maps using the S/N-map and Fig. 6. As a next step we generate a set of simulated σ -maps from the observed maps by randomly shuffling the σ values within the error distribution, and derive the uncertainty in the peak location from the statistics of the Monte-Carlo simulations.

We thus find that the largest uncertainties are related to the spatial sampling of GIRAFFE, i.e., the sub-pixel position adopted for V_{\max} and V_{\min} . In the models this yields a geometrical error of about 0.14 pixels in the location of the peak. For some very extended galaxies (e.g., J033230.78-275455.0 and J033226.23-274222.8), parts of the galaxy fall outside of the IFUs; in these cases, we extrapolated the position of V_{\max} and/or V_{\min} according to the partial VFs and the optical images. Here, we obviously underestimate the corresponding errors. However, most galaxies in the sample are smaller than the field of view of an individual GIRAFFE IFU and are fully sampled; since we are mainly concerned about the ensemble properties of our sample, we did not include this into the total error budget. In total, the uncertainties in the observed σ -map and those found from the models together correspond to an error of 0.14 to 0.8 spatial pixels on Δr , with a median of ~ 0.3 pixels (see Table 2).

The clear distinction between rotating disks and more complex kinematics may serve as additional evidence for the validity of our classification scheme. Galaxies classified as rotating disks are well concentrated near the $\Delta r \sim \epsilon \sim 0$ region, which implies that they are well modeled by a simple rotating disk. Galaxies classified as PR or CK fall outside of this region, and with large scatter. Note that there are five objects with $\Delta r \sim 0$ and $\epsilon > 1$. Their VFs resemble that of a rotation disk, but the amplitude of their σ -peaks show a significant deficiency. Three of them, (J033243.62-275232.6, J033219.32-274514.0 and J033234.12-273953.5) have an obviously disturbed σ -map and VF, which is why we classify them as having perturbed or complex kinematics. The two remaining galaxies (J033233.90-274237.9 and CFR031032) are dominated by bulges that are much bluer than those of present day galaxies and presumably are experiencing star formation (see Neichel et al. 2007). The presence of a star forming bulge may affect the central velocity dispersion in such

a way that a pure rotating disk model underestimates the true σ -peak amplitude. It is then possible that these two galaxies are indeed supported by the combination of a rotation and dispersion, as expected for S0 galaxies.

During the final phase of the classification process (see Table 2), we have indeed used Fig. 4 to verify our results. It had led us to change one galaxy from PR to RD class (J033230.78-275455.0, see discussion above) and one galaxy from RD to PR class (J033248.28-275028.9), thus evidencing that classification errors are marginal. Furthermore, one PR galaxy (J033219.61-274831.0) falls close to the region of rotating disks and has relatively large error bars in Δr (see Fig. 4 and Table 2). Its σ -peak is located near the edge of the σ -map, which causes a relatively large uncertainty on the peak location. However, given the S/N of the σ -peak and the presence of a secondary peak near the galaxy center, there is no doubt about its classification as PR.

3.4. Comments on individual targets

J033212.39-274353.6: Kinematically classified as a RD. The dynamical major axis is aligned with the morphological major axis. The σ -map shows a clear peak near the center.

J033219.68-275023.6: This is an excellent example of a RD. The velocity gradient and the sigma peak are well consistent with a RD, while the morphology clearly shows spiral arms.

J033230.78-275455.0: It has the morphology of a spiral galaxy. Its [OII] emission is relatively faint, and only the lower half of the galaxy was detected. Nevertheless, the peak of the σ -map is well centered on the nucleus of the galaxy. The σ -map is in agreement with our simple rotational model, where the center and PA have been chosen according to the geometry of the optical image. Thus, we classify its VF to be a RD.

J033231.58-274121.6: The kinematics indicates that this is a RD, in spite of its irregular morphology (see Neichel et al. 2007).

J033234.04-275009.7: We find a well ordered velocity gradient consistent with disk rotation, and dispersion peaks near the morphological and kinematic center. Notice that the σ peak falls just between two GIRAFFE pixels. This galaxy is classified as a RD, in spite of its irregular morphology (Neichel et al. 2007).

J033237.54-274838.9: Kinematically, this galaxy appears to be a RD. Morphologically, we find a nearly face-on disk galaxy with an asymmetric outer region and prominent arms. Both the optical images and kinematic maps show the typical features of a rotating system.

J033238.60-274631.4: The VF shows the characteristics of a RD. Morphologically it has been classified as an S0 galaxy. Thus, we classify this galaxy as a RD.

J033241.88-274853.9: A RD with a dynamical axis centered on the luminous peak of the red HST/ACS image. The morphology appears however asymmetric, and this galaxy has been classified as peculiar/tadpole by Neichel et al. (2007). Indeed, the ionized gas detected by the IFU has no stellar counterpart on one side of the galaxy.

J033245.11-274724.0: We classify this galaxy as a RD, in spite of a secondary peak, which is offset from the dispersion map. However, this is a compact object with symmetric spiral arms. The double peak in the dispersion map can be reproduced by our simulation and may be an artefact caused by the relatively low spatial resolution of the data, due to the compactness of the source.

J033210.25-274819.5: The VF is not well aligned with the major axis of the galaxy because of one high S/N pixel with the highest velocity. The σ peak is found to be close to this pixel,

and cannot be reproduced by rotation along the major axis, implying that the rotation is perturbed.

J033214.97-275005.5: The peak of the σ -map significantly deviates from the center of this face-on galaxy, we therefore classify it as a PR.

J033219.61-274831.0: Another PR for which the σ -map shows a peak that is well offset from the dynamical center. Morphologically, this appears to be a peculiar, perhaps merging galaxy (Neichel et al. 2007). In the spectrum with the largest velocity dispersion, we identify a narrow component superimposed onto a broad component. This may be related to merging.

J033226.23-274222.8: The VF of this galaxy is classified as PR. The VF shows the dynamical axis parallel to the morphological major axis. However, the peak in the σ -map is not well aligned with this axis. This perturbed component in the σ -map corresponds to a blue clump in the HST data (Neichel et al. 2007), which might be a gas rich satellite galaxy.

J033232.96-274106.8: The peak in the σ -map is offset from the dynamical axis. Thus, this is clearly a PR. An unresolved component near the bottom left corner of the kinematic maps may correspond to a small companion of this galaxy, which perhaps is the cause of the perturbation.

J033233.90-274237.9: The σ -map shows a peak near the dynamical center. Our rotating disk model can reproduce the σ -peak in position but not its amplitude. The morphological analysis by Neichel et al. (2007) suggests that this is a S0 galaxy with a significant bulge (B/T=0.8). Our purely rotating disk model does not take into account the bulge: if we add a bulge with a typical velocity dispersion of $\sim 50 \text{ km s}^{-1}$, then we are able to reproduce the data. Conservatively, we classify this galaxy as a PR, although the perturbation may simply be caused by the prominent bulge.

J033239.04-274132.4: The dynamical and morphological major axes are aligned, but the peak of the σ -map is strongly offset from the this axis. Its VF is obviously a PR. The center of this galaxy shows very luminous [OII] line emission.

J033243.62-275232.6: Classified as a PR because the σ -map does not show a single peak but a very extended large σ region, which cannot be reproduced with our rotating disk model.

J033248.28-275028.9: The VF is classified as PR. The σ -map shows an elongated peak across two spatial pixels, and has a secondary peak. The extended peak of the σ -map cannot be reproduced by our model of a rotating disk. The overall blue colour (Neichel et al. 2007) of the galaxy may be related to enhanced star-formation as a result of the perturbed gravitational potential.

J033249.53-274630.0: The VF of this galaxy is classified as PR because of the irregularity of its σ -map, which cannot be reproduced assuming pure rotation. The morphological analysis by Neichel et al. (2007) suggests that this may be a merger.

J033250.53-274800.7: We detect that the dynamical axis follows the major axis of the galaxy, but the peak of the σ -map is clearly offset from the center.

J033210.76-274234.6: It is classified to be CK without evidence for a dynamical axis. The peak of the σ -map is not located at the center of the galaxy.

J033213.06-274204.8: It has possibly a spiral morphology (maybe with a bar), but the kinematics are complex. We find the dynamical axis is clearly misaligned with the optical major axis. The σ -map is irregular without any peak at the center, and with an overall relatively high velocity dispersion ($\sim 50 \text{ km s}^{-1}$) over the whole field.

J033217.62-274257.4: The dynamical axis is misaligned with the major axis, implying complex kinematics. We also detected

that a very broad and high dispersion σ -peak covers the majority of the galaxy.

J033219.32-274514.0: Its kinematics is complex. Both VF and σ -map are perturbed. No dynamical axis can be determined from the VF.

J033220.48-275143.9: It clearly shows a CK, from both VF and σ -map patterns.

J033224.60-274428.1: A complex VF, which shows a velocity gradient along one component major axis while the σ -map shows a very large region of high dispersion region that deviates from the center of galaxy. Its morphology resembles that of an on-going merger.

J033225.26-274524.0: The VF shows a well ordered velocity gradient but skewed. Its σ -map does not show any peak near the center. Thus, it was classified to be a CK.

J033227.07-274404.7: We detect a very small velocity gradient over most of the galaxy, with an amplitude of less than 20 km/s. The top end clump in the optical image is responsible for the highest velocity detected. The peak of the σ -map is offset from the center of the galaxy and corresponds to the maximum gradient in the VF. Its VF and coma-like morphology make us suspect that this is a merger between two or three galaxies.

J033228.48-274826.6: Both VF and σ -map show the signs of perturbation. No clear dynamical axis can be found. Its morphology is classified as irregular.

J033230.43-275304.0: Its VF is classified CK, because the dynamical axis is not oriented along the major axis and the VF does not show a clear velocity gradient consistent with rotation. The peak of the σ -map is strongly offset from the center of the galaxy.

J033230.57-274518.2: It is classified as possessing complex kinematics. Its VF shows a very asymmetric gradient while the σ -map shows a clear difference from a single peak pattern.

J033234.12-273953.5: This galaxy has CK. We have detected a narrow VF and a low velocity dispersion for this object. The peak of the σ -map is not corresponding to the center of the galaxy. It has an irregular morphology and a nearby companion, which we do not detect in the [OII] line emission. This may be an on-going merger or a simple projection of two objects at different redshift. We also notice that VVDS misidentified the [OII] emission of this galaxy.

J033239.72-275154.7: This is a galaxy with CK showing no evidence for rotation. Its dynamical axis seems to be parallel to a possible bar-like structure but it is clearly offset from this structure. Because of its low inclination, it is not expected to have a large amplitude of the velocity field. The σ -map shows a peak clearly deviating from the galaxy center.

J033240.04-274418.6: The kinematics are classified as complex. Its VF is perturbed and its σ -map is offset from the center.

J033244.20-274733.5: We find no evidence for rotation in the VF. The σ -map shows a single peak close to the center of galaxy, but the central velocity dispersion is much higher than expected for a rotating system.

J033250.24-274538.9: This is a low surface brightness galaxy with complex kinematics showing no evidence for rotation. Its large large amplitude of the VF is unexpected for such a low inclination system. Both VF and σ -map show deviations from a normal RD.

4. Discussion

Table 3 shows how the galaxies in our sample fall into the different kinematical classes. We find 32% RDs, 25% PRs and 43%

Table 3. Statistics of each kinematical class in different fields for the complete sample (63 galaxies with $M_J(\text{AB}) < -20.3$).

	HDFS	CFRS22h	CFRS03h	CDFS	Total (fraction)
RD	4	2	5	9	20 (32%±12%)
PR	2	2	2	10	16 (25%±12%)
CK	3	2	6	16	27 (43%±12%)
UC	3 in total			3	6 (9%)

Note: the first column gives the kinematical classifications (see Sect. 3.2 for details): RD-rotating disks; PR-perturbed rotations; CK-complex kinematics; UC-unclassified. Five galaxies (CFRS220619, CFRS220919, HDFS4070, HDFS4090, J033243.62-275232.6) are not included in this statistic because they are fainter than the limiting magnitude of $M_J(\text{AB}) = -20.3$.

CKs which are limited by an error of 12%. This confirms the preliminary result of Flores et al. (2006) that at $z = 0.4 - 0.75$, few massive emission line galaxies are kinematically relaxed. Furthermore, the combined two samples include galaxies from 4 different fields, namely the CDFS, HDFS, CFRS03h and CFRS22h. We refer to the later three fields as the GTO sample (see Flores et al. 2006). It is based on 3 different lines of sight, therefore its result is unlikely to be affected by the cosmic variance effect. The GTO sample gives RD:PR:CK = 11:6:11 (i.e., 39%:22%:39%), which is consistent with the results from CDFS (25%:28%:47%) within the statistical error. Notice however that in the field of CDFS we discovered a relatively large fraction of CKs, which is possibly related to the presence of large-scale structure (Ravikumar et al. 2007). In total our sample includes 6 galaxies that are unclassified (UC), because the data are not well resolved spatially. The relatively small fraction of RD galaxies is intriguing, in particular if compared with the significantly larger fraction of disk galaxies found at low redshift (see below). We emphasize the robustness of this result, in particular because:

- the sample is representative of galaxies with $M_{\text{stellar}} \geq 1.5 \times 10^{10} M_{\odot}$ (see Sect. 2.3 and Fig. 2.3);
- it is unaffected by cosmic variance since galaxies are selected from four independent fields, and we find that the fraction of galaxies with a particular classification does not vary significantly from field to field (see Table 3);
- it is based on a representative sample of 63 galaxies, and the uncertainties to the above fractions are smaller than 12%.

Let us now consider the general population of galaxies at $z = 0.4 - 0.75$, with $M_{\text{stellar}} \geq 1.5 \times 10^{10} M_{\odot}$, including emission line galaxies (with $W_0([\text{OIII}]) \geq 15 \text{ \AA}$) like those studied in this paper, and also more quiescent galaxies with very faint or without emission lines (e.g., quiescent late type galaxies such as E/S0 and some early type spirals). Hammer et al. (1997, see also Hammer et al. 2005) have found that at $z = 0.65$ (the average redshift of our sample), 60% of intermediate mass galaxies have emission lines, and this result has been confirmed by all galaxy surveys. We further assume that all quiescent galaxies have relaxed kinematics, e.g., pressure (or dispersion) supported for spheroids and rotationally supported for disks. This implies that at $z = 0.4 - 0.75$, at least $41 \pm 7\%$ of galaxies are not dynamically relaxed, including $26 \pm 7\%$ of galaxies with CKs. This result is in sharp contrast with the kinematics of present-day galaxies, which are almost all relaxed, and indicates a strong evolution over the last 5 Gyr. Indeed, at $z = 0$, we find that 70% of intermediate mass galaxies are spirals, while irregulars, compact galaxies and mergers contribute to less than 1% (e.g., Hammer et al. 2005).

This result is unlikely to be affected by artefacts of our methodology. To illustrate this, we will now critically evaluate the possible sources of error leading to misclassifications, and quantify their impact on the ensemble properties of our sample.

As discussed earlier (Sect. 3.4), we suspect that two galaxies classified as a perturbed rotation may in fact have an enhanced central velocity dispersion due to the effect of a prominent star-forming, and possibly gas-rich, bulge. This does not change our result significantly, as it would only reduce the fraction of kinematically perturbed galaxies from 41% to 39%. Moreover, for objects with small spatial coverage, i.e., galaxies extending over less than 6 spatial pixels, our classification may be less robust than for more extended galaxies. This is the case for a few compact galaxies, in particular those with half light radii less than one GIRAFFE pixel ($0.52''$), and for a few more extended galaxies that have relatively weak emission (i.e., a mean S/N < 4). However, these galaxies represent less than 10% of the whole sample. For more than 90% of the sample, the kinematics are well sampled, with a median spatial coverage of 9 pixels at S/N > 4), allowing us to robustly and uniquely classify the kinematics. We note explicitly that we verified that the classification does not depend on the mean S/N of the galaxies. Moreover, Flores et al. (2006) and Puech et al. (2007) have convincingly shown that galaxies with non-relaxed kinematics are responsible for the large dispersions of both the Tully-Fisher and the $J_{\text{disk}} - V_{\text{max}}$ relationships. So it is beyond doubt that a significant fraction of $z = 0.4 - 0.75$ galaxies have kinematics that deviate significantly from those of their local descendants, i.e., the present-day intermediate-mass galaxies, which include 70% of spirals.

Which physical process could explain such a dramatic evolution in the kinematics of galaxies within a relatively modest amount of time (4–7 Gyr)? The morphology of several galaxies in the sample strongly advocates that merging is one such process. For example, a minor merger may cause perturbed rotation: the in-fall of a gas-rich satellite would unavoidably lead to a local increase of the dispersion shifting the peak of the σ -map. A major merger will significantly affect a rotational VF by destroying the pre-existing disk, and lead to a signature resembling a complex VF (see Puech et al. 2006a and 2007). It is then probable that merging may explain most of the discrepancies in the observed VFs at $z = 0.4 - 0.75$. However, this fact alone does not necessarily imply that merging is the only physical process explaining the strong evolution of galaxy kinematics.

If major mergers are responsible for complex VFs, then $26 \pm 7\%$ of the galaxies within $z = 0.4 - 0.75$ will either be on-going mergers or merger remnants. This has to be compared with only $5 \pm 1\%$ of on-going mergers, as revealed by pair counts, two-point correlation or morphological classifiers (see a summary in Hammer et al. 2007 and references therein). Indeed, these morphological analyzes essentially account for the approaching phase of a merger, while kinematics are affected by large scale peculiar motions induced before and after the merger. This leads Hammer et al. (2007) to postulate that the merger remnant phase may be 4 to 5 times longer than the approaching phase. Assuming $0.35 - 0.4$ Gyr for the duration of the latter, this

results in a merger remnant phase with a duration of 1.5–2 Gyrs. Indeed, simulations by Robertson et al. (2006) and Governato et al. (2007) predict such a duration for the rebuilding of a disk after a major merger of gas rich galaxies. Furthermore, the requirement for gas rich interacting galaxies in Robertson et al. (2006), finds some support from the evolution of the gas content in galaxies as a function of cosmic time, although this evolution is derived indirectly from the gas phase metal abundance in distant galaxies. Liang et al. (2006) estimated that the gas content in intermediate-mass galaxies at $z \sim 0.6$ was two times larger than in galaxies at the current epoch.

However, the predominance of mergers, and especially major mergers, leads to the requirement that many present-day galactic disks have in fact been rebuilt at a relatively recent epoch. Taking into account the number fraction of both on-going mergers and galaxies with complex VFs, Hammer et al. (2005, 2007) conclude that between 50% and 70% of galaxies may have experienced a major merger and subsequent disk rebuilding since $z = 1$. Although this alternative may explain many observations in the $z = 0.4 - 1$ redshift range (e.g., Hammer et al. 2005), could a less dramatic mechanism be at the origin of the peculiar kinematics $z = 0.4 - 0.75$?

In fact our observations can only account for the large scale motions traced by the ionized gas and not those of the stellar component. Observations of the latter are certainly crucial, although for most distant galaxies this is beyond the reach of 8 to 10 meter telescopes. One may then postulate that rapid gas motions may be superimposed on a normal rotational stellar component. There are two difficulties with such an assumption. First, at $z = 0.4 - 0.75$ the gaseous fraction is much higher than today, and represents a significant fraction of the baryonic mass. To illustrate this, recall that since $z = 1$, about half of the present-day stellar mass has been formed from gas in intermediate mass galaxies (Hammer et al. 2005; Bell et al. 2005). One may then wonder how under such conditions an ordered rotational VF of about half of the baryons (stars) may survive against highly perturbed VFs for the other half of the baryons (gas). The origin of a large-scale motion gas component is certainly a second difficulty, especially if no merger is advocated. Another possibility may be to invoke internal processes, such as bars, that may perturb the gaseous VFs. One may wonder whether the presence of bars in the central region could create additional dispersion leading to apparently unrelaxed VFs according to our VF diagnostic (see Fig. 4). However, our spatial resolution may be too poor to kinematically characterize most of the bars, except possibly the most giant ones. Could some vigorously enhanced internal processes contribute to the complex VFs? Indeed, this is not expected from the apparent non-evolution of the frequency of barred galaxies (e.g., Zheng et al. 2005 and references therein), which does not support that bars are the process to explain the large evolution of galaxy kinematics. The observed motions at large scales rather suggest another mechanism, probably related to asymmetric gas accretions (such as provided by a merger) or perhaps to gas outflows.

5. Conclusion

We have been able to measure the VFs of 36 galaxies at $z = 0.4 - 0.75$ using deep exposures of the multiplex integral-field spectrograph GIRAFFE at the VLT in the multi-IFU mode, measuring the kinematics of the spatially and spectrally well resolved [OII] emission line doublet. In combination with a similar study by Flores et al. (2006), we have a relatively large and representative sample of 63 galaxies with $M_{\text{stellar}} \geq 1.5 \times$

$10^{10} M_{\odot}$. Thus, our results are representative for the population of intermediate-mass galaxies in this redshift range, and it cannot be affected by cosmic variance. To date, this is the only existing representative sample of distant galaxies with measured VFs.

We confirm and consolidate the results of Flores et al. (2006), that a significant fraction of intermediate mass galaxies had perturbed or complex kinematics 5 Gyrs ago. Our method to classify the kinematics of the galaxies is particularly robust. It attributes a large weight to the velocity dispersion in the central region of the galaxy, where the S/N are the highest. Even if we assume that all quiescent galaxies at $z = 0.4 - 0.75$ had well ordered VFs, we find that $41 \pm 7\%$ of the galaxies are not kinematically relaxed, including $26 \pm 7\%$ of galaxies that show complex kinematics. Undoubtedly, galaxy kinematics are evolving very rapidly, since most present-day galaxies in the same mass range are likely to have ordered VFs.

This result may be combined with the fact that anomalous VFs are responsible for most of the large observed dispersion of both the Tully-Fisher and the $j_{\text{disk}} - V_{\text{max}}$ relationships (see Flores et al. 2006 and Puech et al. 2007). It suggests a random walk evolution of galaxies related to a high fraction of merging events, including major mergers (Puech et al. 2007). Mergers may indeed reproduce all the peculiar kinematics at $z = 0.4 - 0.75$, as well as being responsible for the dispersion of fundamental relations. Other mechanisms, such as in-fall of high velocity gas clouds, gas outflows or bars may also contribute to the observed evolution in the kinematics. To understand their influences, and moreover the underlying mechanisms that activate them, requires detail analyzes of individual objects and as a prerequisite, a full model of the significance of the GIRAFFE measurements. If major merging is the main mechanism responsible for the large fraction of complex VFs, then this implies that, since $z = 1$, from 50% to 70% of intermediate mass galaxies have experienced a major merger. This is quantitatively in good agreement with the spiral rebuilding scenario as proposed by Hammer et al. (2005).

Acknowledgements. We would like to thank the referee for helpful comments and discussions on the paper. We thank all the GIRAFFE team at the Observatories in Paris and Geneva, and ESO for this unique instrument. We are grateful to Albrecht Rüdiger for helping us in the writing of the paper. We thank Francoise Combes and Denis Burgarella for their useful comments and for their kind support of this program since the beginning, as well as Andrea Cimatti, Emanuele Daddi, David Elbaz, Olivia Garrido, Dominique Proust, Xianzhong Zheng.

References

- Barnes, J. E., & Hernquist, L. 1996, ApJ, 471, 115
- Barton, E. J., Geller, M. J., & Kenyon, S. J. 2000, ApJ, 530, 660
- Bell, E. F., McIntosh, D. H., Katz, N., & Weinberg, M. D. 2003, ApJS, 149, 289
- Bell, E. F., et al. 2005, ApJ, 625, 23
- Bell, E. F., Phleps, S., Somerville, R. S., Wolf, C., Borch, A., & Meisenheimer, K. 2006, ApJ, 652, 270
- Bertin, E., Arnouts, S. 1996, A&AS, 117, 393
- Conselice, C. J., Gallagher, J. S., III, & Wyse, R. F. G. 2003, AJ, 125, 66
- Conselice, C. J., Bundy, K., Ellis, R. S., Brichmann, J., Vogt, N. P., & Phillips, A. C. 2005, ApJ, 628, 160
- Cowie, L. L., Songaila, A., & Barger, A. J. 1999, AJ, 118, 603
- Dressler, A. 2004, Clusters of Galaxies: Probes of Cosmological Structure and Galaxy Evolution, 206
- Ferreras, I., & Silk, J. 2001, ApJ, 557, 165
- Ferreras, I., Silk, J., Böhm, A., & Ziegler, B. 2004, MNRAS, 355, 64
- Flores, H., et al. 1999, ApJ, 517, 148
- Flores, H., Hammer, F., Puech, M., Amram, P., & Balkowski, C. 2006, A&A, 455, 107
- Fuentes-Carrera, I., et al. 2004, A&A, 415, 451
- Giovanelli, R., Haynes, M. P., da Costa, L. N., Freudling, W., Salzer, J. J., & Wegner, G. 1997, ApJ, 477, L1
- Governato, F., Willman, B., Mayer, L., Brooks, A., Stinson, G., Valenzuela, O., Wadsley, J., & Quinn, T. 2007, MNRAS, 374, 1479

- Guzman, R. 1999, in Proc. 19th Moriond Conf., Building Galaxies: From the Primordial Universe to the Present, ed. F. Hammer, T. X. Thuan, V. Cayatte, B. Guiderdoni, & J. T. T. Van (Paris: Editions Frontiers), 269
- Haarsma, D. B., Partridge, R. B., Windhorst, R. A., & Richards, E. A. 2000, *ApJ*, 544, 641
- Hammer, F., et al. 1997, *ApJ*, 481, 49
- Hammer, F., Gruel, N., Thuan, T. X., Flores, H., & Infante, L. 2001, *ApJ*, 550, 570
- Hammer, F., Flores, H., Elbaz, D., Zheng, X. Z., Liang, Y. C., & Cesarsky, C. 2005, *A&A*, 430, 115
- Hammer, F., Puech, M., Chemin, L., Flores, H., & Lehnert, M. 2007, *ArXiv Astrophysics e-prints*, arXiv:astro-ph/0702585
- Heavens, A., Panter, B., Jimenez, R., & Dunlop, J. 2004, *Nature*, 428, 625
- Hernández-Toledo, H. M., Fuentes-Carrera, I., Rosado, M., Cruz-González, I., Franco-Balderas, A., & Dultzin-Hacyan, D. 2003, *A&A*, 412, 669
- Hopkins, A. M. 2004, *ApJ*, 615, 209
- Kannappan, S. J., & Barton, E. J. 2004, *AJ*, 127, 2694
- Koo, D. C., Guzman, R., Faber, S. M., Illingworth, G. D., Bershadsky, M. A., Kron, R. G., & Takamiya, M. 1995, *ApJ*, 440, L49
- Le Fèvre, O., et al. 2000, *MNRAS*, 311, 565
- Liang, Y. C., Hammer, F., & Flores, H. 2006, *A&A*, 447, 113
- Lilly, S. J., Le Fèvre, O., Hammer, F., & Crampton, D. 1996, *ApJ*, 460, L1
- Lotz, J. M., Madau, P., Giavalisco, M., Primack, J., & Ferguson, H. C. 2006, *ApJ*, 636, 592
- Madau, P., Ferguson, H. C., Dickinson, M. E., Giavalisco, M., Steidel, C. C., & Fruchter, A. 1996, *MNRAS*, 283, 1388
- Neichel et al. 2007, in preparation
- Noeske, K. G., Koo, D. C., Phillips, A. C., Willmer, C. N. A., Melbourne, J., Gil de Paz, A., & Papaderos, P. 2006, *ApJ*, 640, L143
- Östlin, G., Amram, P., Bergvall, N., Masegosa, J., Boulesteix, J., & Márquez, I. 2001, *A&A*, 374, 800
- Portinari, L., & Sommer-Larsen, J. 2007, *MNRAS*, 375, 913
- Pozzetti, L., et al. 2003, *A&A*, 402, 837
- Puech, M., Flores, H., Hammer, F., & Lehnert, M. D. 2006a, *A&A*, 455, 131
- Puech, M., Hammer, F., Flores, H., Östlin, G., & Marquart, T. 2006b, *A&A*, 455, 119
- Puech, M., Hammer, F., Lehnert, M. D., & Flores, H. 2007, *A&A*, 466, 83
- Ravikumar, C. D., et al. 2007, *A&A*, 465, 1099
- Rawat, A., Kembhavi, A. K., Hammer, F., Flores, H., & Barway, S. 2007, *ArXiv e-prints*, 704, arXiv:0704.2177
- Robertson, B., Bullock, J. S., Cox, T. J., Di Matteo, T., Hernquist, L., Springel, V., & Yoshida, N. 2006, *ApJ*, 645, 986
- Tully, R. B., & Fisher, J. R. 1977, *A&A*, 54, 661
- Weiner, B. J., et al. 2006, *ApJ*, 653, 1027
- Werk, J. K., Jangren, A., & Salzer, J. J. 2004, *ApJ*, 617, 1004
- Wilson, G., Cowie, L. L., Barger, A. J., & Burke, D. J. 2002, *AJ*, 124, 1258
- Zheng, X. Z., Hammer, F., Flores, H., Assémat, F., & Rawat, A. 2005, *A&A*, 435, 507